Generalized Predictive Direct Power Control With Constant Switching Frequency for Multilevel Four-Leg Grid Connected Converter

Mansour Bouzidi, *Member, IEEE*, Said Barkat, Abdelbasset Krama, *Member, IEEE*, and Haitham Abu-Rub, *Fellow, IEEE*

***Abstract*—This article proposes a novel generalized predictive direct power control (PDPC) with a constant switching frequency for a multilevel four-leg (4L) grid connected converter (GCC) diode clamped converter (DCC). A new predictive power model for 4L-GCC is developed in which the proposed PDPC can operate with a constant switching frequency without any modulation stage. During each switching period, four appropriate switching vectors are selected and applied using precalculated switching times. Moreover, these appropriate switching vectors are selected only from one sector, and a new proposed approach to calculate the switching times is proposed and generalized for any level of 4L-DCC. The proposed PDPC for the multilevel 4L-GCC can ensure better active and reactive powers control, lower grid current harmonics, better compensation of grid neutral current and reactive power, and accurate balancing of the dc capacitor voltages. The presented results demonstrate the effectiveness of the proposed control strategy.**

***Index Terms*—Active and reactive powers, four-leg converter, generalized predictive direct power control (PDPC), multilevel converter, predictive direct power control (DPC).**

I. Introduction

In RECENT years, voltage source converters (VSCs) are immensely used in the modern power system to meet the requirement of renewable energy dominated grid [1], [2]. One of the major key functions of grid connected converter (GCC) is to ensure energy conversion and control the power flow between the dc side and the grid side. In the distributed power generation systems, the four-leg (4L) topology of the VSCs presents the best option to deal with unbalanced grid voltages and currents [3]–[6]. Such topology provides many advantages, such as the ability to supply three-phase and single-phase loads at the same time, full utilization of the dc-link voltage, and capability to handle unbalanced load [3]–[6]. Therefore, the use of four-leg voltage source converters (4L-VSIs) as grid interface has become increasingly attractive for different applications, such as renewable energy (e.g., wind energy, solar energy, etc.) [6], active power filters [3], and microgrid applications [4].

Many research works have been focused on developing control strategies of the GCC–VSC to improve its efficiency, reliability, and safety [7]–[11]. Among those control strategies is the direct power control (DPC), which has received considerable scholarly attention in recent years [9]–[11]. In DPC, the active and reactive powers are controlled directly without any inner current control loop or pulsewidth modulation (PWM) block [9]. However, the major drawback of this control strategy is the variable switching frequency (VSF) [10], [12]. Hence, in order to operate with a constant switching frequency (CSF), some works used the space vector modulation (SVM) block [10], [12]. Moreover, in [13] and [14], the sliding-mode control and passivity-based control are combined with DPC with the aim to get more robustness and higher performance. However, the above-mentioned control strategies present significant power ripples in the active and reactive powers.

Different structures of the DPC based on predictive approaches, i.e., predictive direct power control (PDPC), have been widely utilized [15]–[24]. The PDPC strategies can be classified into two categories: VSF and CSF. In the first category, the converter's switching states are selected through the minimization of a predefined cost function [15]–[17]. However, in such approach, the control performance is strongly dependent on the sampling frequency and filter parameters. In the second category, the switching frequency is ensured by SVM block. However, the calculation of the average output voltage is issued by the predictive model as in the previous approach [22], [23].

An interesting PDPC algorithm operating with a CSF without using PWM block has been proposed in [18]–[21]. This control strategy is based on applying, during each switching period, three switching vectors (SWVs) using precalculated switching times. The switching times are calculated by minimizing a cost function, which ensures the convergence of the active and reactive powers to their reference values [18]–[21]. This

Manuscript received August 10, 2021; revised November 13, 2021; accepted December 24, 2021. Date of publication January 11, 2022; date of current version February 18, 2022. This work was supported by Qatar National Research Fund (a member of Qatar Foundation) under Grant NPRP12S-0226-190158. Recommended for publication by Associate Editor Z. Zhang. *(Corresponding author: Abdelbasset Krama.)*

Mansour Bouzidi is with the Department of Electronics and Telecommunications, University of Kasdi Merbah, Ouargla 30000, Algeria (e-mail: bouzidi.mansour@univ-ouargla.dz).

Said Barkat is with Electrical Engineering Laboratory, University of M'sila, M'sila 28000, Algeria (e-mail: said.barkat@univ-msila.dz).

Abdelbasset Krama and Haitham Abu-Rub are with the Department of Electrical and Computer Engineering, Texas A&M University at Qatar, Doha 23874, Qatar (e-mail: krama.abdelbasset@qatar.tamu.edu; haitham.abu-rub@qatar.tamu.edu).

Color versions of one or more figures in this article are available at https://doi.org/10.1109/TPEL.2022.3142113.

Digital Object Identifier 10.1109/TPEL.2022.3142113

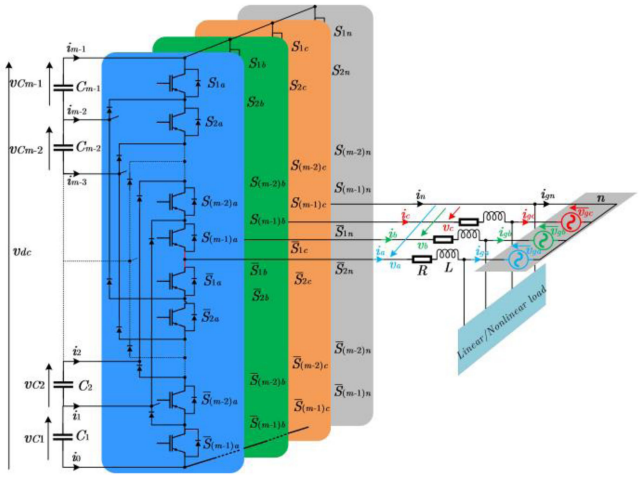

Fig. 1. Multilevel 4L-DCC connected to GCC via *R–L* filter.

control strategy provides good results in terms of power ripples, waveforms quality, and time response. In addition, it operates with CSF without using any modulation stage. However, this control strategy has been applied only in three-phase three-leg two-level and three-level VSCs. To the best of authors' knowledge, there is no work that has performed this kind of PDPC for 4L-VSCs, as there is no available predictive power model for 4L-VSC. Furthermore, the PDPC algorithm for 4L-VSCs will become more complicated when the number of VSC levels increases.

Therefore, in this article, a simplified and generalized PDPC operated with a CSF for multilevel 4L-GCC based on a new predictive power model is proposed. In the proposed PDPC, a new method of calculating switching times is presented and generalized for any four-leg diode clamped converter (4L-DCC) level. The proposed PDPC can guarantee accurate control of active/reactive powers, zero-sequence current, grid neutral current, as well as balancing the dc capacitor voltages for multilevel 4L-DCC.

The contribution of the article is summarized as the following.

1) Generalizing the PDPC with a CSF for multilevel 4L-GCC.
2) Developing a new predictive power model for 4L-GCC.
3) Proposing a new method for the switching times calculation.

The rest of this article is organized as follows. In Section II, the power circuit describing the *m*-level 4L-GCC and its mathematical model is presented. The proposed generalized PDPC with a CSF strategy is presented and discussed deeply in Section III. In Section IV, the effectiveness of the proposed PDPC-CSF is verified, compared, and validated experimentally. Finally, Section V concludes this article.

II. Modeling of Grid Connected 4L-DCC

Fig. 1 shows the *m*-level 4L-DCC-based GCC. In this article, the dc side of the 4L-DCC is supplied by a fixed dc source, while the capacitors' voltages balancing is ensured by the proposed control strategy.

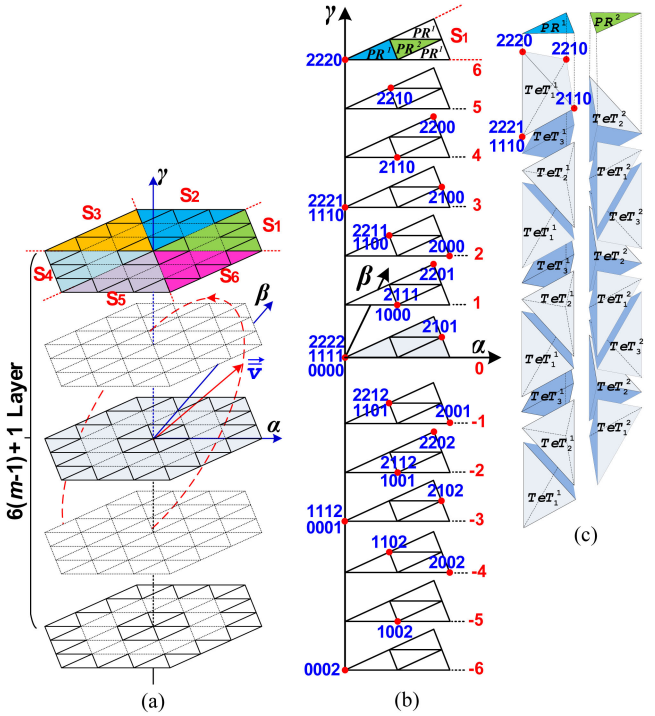

Fig. 2. Three-dimensional representation of the SVD. (a) For *m*-level 4L-DCC. (b) First sector with switching states of three-level 4L-DCC. (c) Tetrahedrons of prisms PR^1 and PR^2 for three-level 4L-DCC.

The dynamic equations of the converter output current $i_{\alpha\beta\gamma}$ in the stationary reference frame $\alpha\beta\gamma$ can be expressed as the function of the output converter voltages $v_{\alpha\beta\gamma}$ and grid voltages $v_{g,\alpha\beta\gamma}$, as follows:

$$di_{\alpha\beta\gamma}/dt = (v_{\alpha\beta\gamma} - v_{g,\alpha\beta\gamma} - Ri_{\alpha\beta\gamma})/L. \tag{1}$$

The output to neutral voltages v_a, v_b, and v_c of the *m*-level 4L-DCC can be estimated as follows:

$$v_x = \sum_{j=0}^{m-1} \left[(F_{xj} - F_{nj}) \sum_{i=1}^{j} v_{C_i} \right], x = a, b, \text{or } c \tag{2}$$

where v_{Ci} is the voltage of the capacitor C_i, and F_{xj} are the switching functions.

The *m*-level 4L-DCC has m^4 possible switching combinations, which can be stored into $6(m-1)+1$ layers in $\alpha\beta\gamma$ space [see Fig. 2(a)]. The SVD of Fig. 2(a) can be divided into six sectors; each sector further is divided into $(m-1)^2$ prisms (PR) and each prism is formed by tetrahedrons (TeT) ([see Fig. 2(b) and (c)], example of three-level 4L-DCC).

III. Proposed Generalized PDPC for *M*-Level 4L-GCC

Fig. 3 shows the block diagram of the proposed PDPC for the *m*-level 4L-DCC connected to the grid. The proposed scheme is based on defining a new predictive power model for the 4L-DCC in the first sector of the SVD of Fig. 2(a).

The grid voltage vector $\vec{v}_g$, the line current vector $\vec{i}_g$, the converter current vector $\vec{i}$, as well as the average output voltage

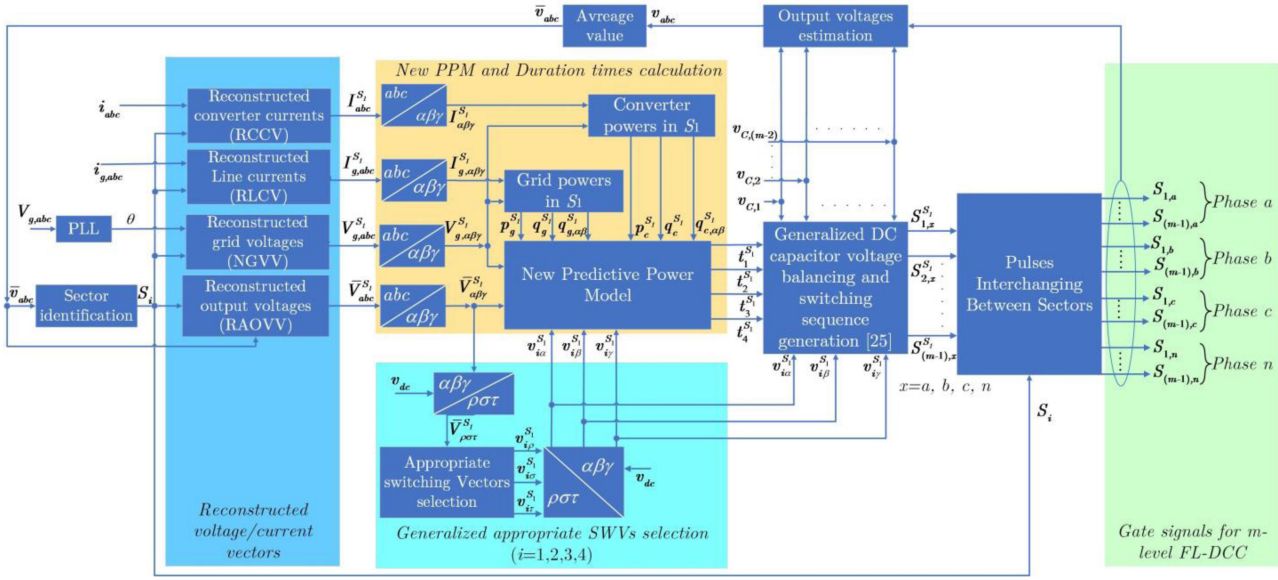

Fig. 3. Block diagram of the proposed generalized PDPC with a CSF for *m*-level grid connected 4L-DCC.

vector $\vec{v}$ are used to create the corresponding vectors, which are noted as follows:

1) reconstructed grid voltage vector $\vec{V}_g^{S_1}$;
2) reconstructed line current vector $\vec{I}_g^{S_1}$;
3) reconstructed converter current vector $\vec{I}^{S_1}$;
4) reconstructed average output voltage vector $\vec{\bar{V}}^{S_1}$.

These reconstructed vectors must only rotate in the first sector and must take all the information about the corresponding vectors $(\vec{v}_g, \vec{i}_g, \vec{i}, \vec{v})$ in other sectors. The reason of using these reconstructed vectors is to simplify the proposed PDPC through selecting the appropriate SWVs only from the first sector of the space vector diagram (SVD) of Fig. 2(a). The reconstructed vectors are used to define the new predictive power model and to calculate the grid powers $p_g^{S_1}$, $q_g^{S_1}$, $q_{g,\alpha\beta}^{S_1}$ and converter powers $p_c^{S_1}$, $q_c^{S_1}$, $q_{c,\alpha\beta}^{S_1}$.

Based on the location of the reconstructed voltage vector $\vec{\bar{V}}^{S_1}$ in the first sector, the four adjacent vectors of $\vec{\bar{V}}^{S_1}$ are selected as the appropriate SWVs to be applied at each switching period T_{sw}. The selection of the appropriate SWVs is generalized for any level of the 4L-DCC based on the adopted method proposed in [25]. The corresponding switching times are calculated based on a new generalized approach for *m*-level 4L-GCC.

A. Reconstructed Voltage/Current Vectors

The proposed predictive power model for the 4L-GCC should be identified only in the first sector S_1 of the SVD, therefore, the ac magnitudes needed for the proposed PDPC (see Fig. 3) must be reconstructed to rotate only in S_1. This concept has been proposed by Bouzidi *et al.* [25] to create only the new reference voltage vector in order to simplify the 3-D SVM.

This article shows that the idea presented in [25] can be extended and applied for the voltage and current vectors $\vec{v}$, $\vec{v}_g$, $\vec{i}_g$, and $\vec{i}$ to create their corresponding reconstructed vectors $\vec{\bar{V}}^{S_1}$, $\vec{V}_g^{S_1}$, $\vec{I}_g^{S_1}$, and $\vec{I}^{S_1}$. In [25], there is only one voltage vector that was reconstructed (called new reference voltage vector $\vec{U}^*$), therefore, the components of $\vec{U}^*(U_a^*, U_b^*, U_c^*)$were deduced based on the sector number that contains the reference voltage vector $\vec{v}^*$ (the reference vector before reconstruction) and its components (v_a^*, v_b^*, v_c^*). In this article, there are four vectors to be reconstructed $\vec{v}$, $\vec{v}_g$, $\vec{i}_g$, and $\vec{i}$, and the key point here is to use the sector number that contains only one of them.

Since the average voltage vector $\vec{v}$ represents the voltage vector that can control the converter's active and reactive powers flow, the sector number that contains this vector $(\vec{v})$ will be chosen to create the following ($\vec{\bar{V}}^{S_1}$, $\vec{V}_g^{S_1}$, $\vec{I}_g^{S_1}$, and $\vec{I}^{S_1}$).

Based on the components of the vectors $\vec{v}$, $\vec{v}_g$, $\vec{i}_g$, $\vec{i}$ and the sector number S_i that contains $\vec{v}$, the reconstructed vectors are identified as given in Table I.

To perform the proposed PDPC, the reconstructed voltage/current vectors $\vec{\bar{V}}^{S_1}$, $\vec{V}_g^{S_1}$, $\vec{I}_g^{S_1}$, and $\vec{I}^{S_1}$ are used instead of the corresponding vectors $\vec{v}$, $\vec{v}_g$, $\vec{i}_g$, and $\vec{i}$ in the following sections:

1) to calculate converter and grid active and reactive powers;
2) to develop the new predictive power model;
3) to calculate the switching times of the appropriate SWVs (see Fig. 3).

B. Proposed New Predictive Power Model of 4L-GCC

In this section, a new predictive power model of the 4L-GCC is developed, which is defined only in the first sector S_1 of the SVD of Fig. 2(a).

When the reconstructed voltage/current vectors are used in the inverter output current dynamic equations, (1) becomes as

TABLE I
SELECTION OF THE RECONSTRUCTED VOLTAGE/CURRENT VECTOR COMPONENTS IN *ABC* COORDINATES SYSTEM

Reconstructed vectors components		Sector number that contains the average output voltage vector $\vec{\bar{v}}$					
		S_1	S_2	S_3	S_4	S_5	S_6
$\vec{\bar{V}}^{S_1}$	$\bar{V}_a^{S_1}$	$\bar{v}_a$	$\bar{v}_b$	$\bar{v}_b$	$\bar{v}_c$	$\bar{v}_c$	$\bar{v}_a$
	$\bar{V}_b^{S_1}$	$\bar{v}_b$	$\bar{v}_a$	$\bar{v}_c$	$\bar{v}_b$	$\bar{v}_a$	$\bar{v}_c$
	$\bar{V}_c^{S_1}$	$\bar{v}_c$	$\bar{v}_c$	$\bar{v}_a$	$\bar{v}_a$	$\bar{v}_b$	$\bar{v}_b$
$\vec{V}_g^{S_1}$	$V_{ga}^{S_1}$	v_{ga}	v_{gb}	v_{gb}	v_{gc}	v_{gc}	v_{ga}
	$V_{gb}^{S_1}$	v_{gb}	v_{ga}	v_{gc}	v_{gb}	v_{ga}	v_{gc}
	$V_{gc}^{S_1}$	v_{gc}	v_{gc}	v_{ga}	v_{ga}	v_{gb}	v_{gb}
$\vec{I}_g^{S_1}$	$I_{ga}^{S_1}$	i_{ga}	i_{gb}	i_{gb}	i_{gc}	i_{gc}	i_{ga}
	$I_{gb}^{S_1}$	i_{gb}	i_{ga}	i_{gc}	i_{gb}	i_{ga}	i_{gc}
	$I_{gc}^{S_1}$	i_{gc}	i_{gc}	i_{ga}	i_{ga}	i_{gb}	i_{gb}
$\vec{I}^{S_1}$	$I_a^{S_1}$	i_a	i_b	i_b	i_c	i_c	i_a
	$I_b^{S_1}$	i_b	i_a	i_c	i_b	i_a	i_c
	$I_c^{S_1}$	i_c	i_c	i_a	i_a	i_b	i_b

follows:

$$dI_{\alpha\beta\gamma}^{S_1}/dt = (\bar{V}_{\alpha\beta\gamma}^{S_1} - V_{g,\alpha\beta\gamma}^{S_1} - RI_{\alpha\beta\gamma}^{S_1})/L\ . \tag{3}$$

Using the components of the $\vec{V}_g^{S_1}$ and $\vec{I}^{S_1}$, the converter active and reactive powers defined in the first sector S_1 are given as follows:

$$\begin{bmatrix} p_c^{S_1} \\ q_c^{S_1} \\ q_{c,\alpha\beta}^{S_1} \end{bmatrix} = \begin{bmatrix} V_{g\alpha}^{S_1} & V_{g\beta}^{S_1} & 0 \\ -V_{g\beta}^{S_1} & V_{g\alpha}^{S_1} & 0 \\ 0 & 0 & V_{g\beta}^{S_1} - V_{g\alpha}^{S_1} \end{bmatrix} \begin{bmatrix} I_\alpha^{S_1} \\ I_\beta^{S_1} \\ I_\gamma^{S_1} \end{bmatrix} \tag{4}$$

where $p_c^{S_1}$ and $q_c^{S_1}$ are the converter active and reactive powers defined only in S_1, respectively, and $q_{c,\alpha\beta}^{S_1}$ is the reactive power related to the zero-sequence current, defined as well in S_1.

The derivatives of the converter active and reactive powers defined in (4) are given as follows:

$$\begin{aligned} \dot{p}_c^{S_1} &= I_\alpha^{S_1}\dot{V}_{g\alpha}^{S_1} + V_{g\alpha}^{S_1}\dot{I}_\alpha^{S_1} + I_\beta^{S_1}\dot{V}_{g\beta}^{S_1} + V_{g\beta}^{S_1}\dot{I}_\beta^{S_1} \\ \dot{q}_c^{S_1} &= -I_\alpha^{S_1}\dot{V}_{g\beta}^{S_1} - V_{g\beta}^{S_1}\dot{I}_\alpha^{S_1} + I_\beta^{S_1}\dot{V}_{g\alpha}^{S_1} + V_{g\alpha}^{S_1}\dot{I}_\beta^{S_1} \\ \dot{q}_{c,\alpha\beta}^{S_1} &= I_\gamma^{S_1}\dot{V}_{g\beta}^{S_1} + V_{g\beta}^{S_1}\dot{I}_\gamma^{S_1} - I_\gamma^{S_1}\dot{V}_{g\alpha}^{S_1} - V_{g\alpha}^{S_1}\dot{I}_\gamma^{S_1}. \end{aligned} \tag{5}$$

By neglecting the change of the grid voltages over a sampling period T_s and using (3), the discretization of (5) yields

$$\begin{aligned} \Delta p_c^{S_1}(k) = T_s \Big[& V_{g\alpha}^{S_1}(k)\left(\bar{V}_\alpha^{S_1}(k) - V_{g\alpha}^{S_1}(k) - RI_\alpha^{S_1}(k)\right) \\ & + V_{g\beta}^{S_1}(k)\left(\bar{V}_\beta^{S_1}(k) - V_{g\beta}^{S_1}(k) - RI_\beta^{S_1}(k)\right)\Big]/L \end{aligned} \tag{6.a}$$

$$\begin{aligned} \Delta q_c^{S_1}(k) = -T_s \Big[& V_{g\beta}^{S_1}(k)\left(\bar{V}_\alpha^{S_1}(k) - V_{g\alpha}^{S_1}(k) - RI_\alpha^{S_1}(k)\right) \\ & + V_{g\alpha}^{S_1}(k)\left(\bar{V}_\beta^{S_1}(k) - V_{g\beta}^{S_1}(k) - RI_\beta^{S_1}(k)\right)\Big]/L \end{aligned} \tag{6.b}$$

$$\begin{aligned} \Delta q_{c,\alpha\beta}^{S_1}(k) = T_s \Big[& V_{g\beta}^{S_1}(k)\left(\bar{V}_\gamma^{S_1}(k) - V_{g\gamma}^{S_1}(k) - RI_\gamma^{S_1}(k)\right) \\ & - V_{g\alpha}^{S_1}(k)\left(\bar{V}_\gamma^{S_1}(k) - V_{g\gamma}^{S_1}(k) - RI_\gamma^{S_1}(k)\right)\Big]/L \end{aligned} \tag{6.c}$$

where $\Delta p_c^{S_1}$, $\Delta q_c^{S_1}$, and $\Delta q_{c,\alpha\beta}^{S_1}$ are the converter active and reactive powers' differentials, which are given as follows:

$$\begin{aligned} \Delta p_c^{S_1}(k) &= p_c^{S_1}(k+1) - p_c^{S_1}(k) \\ \Delta q_c^{S_1}(k) &= q_c^{S_1}(k+1) - q_c^{S_1}(k) \\ \Delta q_{c,\alpha\beta}^{S_1}(k) &= q_{c,\alpha\beta}^{S_1}(k+1) - q_{c,\alpha\beta}^{S_1}(k). \end{aligned} \tag{7}$$

At the next sampling period, the active and reactive powers should converge to their reference values $p_c^{*S_1}$, $q_c^{*S_1}$, and $q_{c,\alpha\beta}^{*S_1}$, which means that

$$\begin{aligned} p_c^{S_1}(k+1) &= p_c^{*S_1}(k+1) \\ q_c^{S_1}(k+1) &= q_c^{*S_1}(k+1) \\ q_{c,\alpha\beta}^{S_1}(k+1) &= q_{c,\alpha\beta}^{*S_1}(k+1). \end{aligned} \tag{8}$$

After more simplification, the final new predictive power model is given as follows:

$$\begin{aligned} p_c^{*S_1}(k+1) - p_c^{S_1}(k) &= T_s\left(-R\,p_c^{S_1}(k) + U_\alpha^{S_1}(k)\right)/L \\ q_c^{*S_1}(k+1) - q_c^{S_1}(k) &= T_s\left(-R\,q_c^{S_1}(k) + U_\beta^{S_1}(k)\right)/L \\ q_{c,\alpha\beta}^{*S_1}(k+1) - q_{c,\alpha\beta}^{S_1}(k) &= T_s\left(-R\,q_{c,\alpha\beta}^{S_1}(k) + U_\gamma^{S_1}(k)\right)/L \end{aligned} \tag{9}$$

where $\vec{U}^{S_1}(U_\alpha^{S_1}U_\beta^{S_1}U_\gamma^{S_1})$ is the reconstructed intermediate output voltage vector defined as

$$\begin{aligned} \begin{bmatrix} U_\alpha^{S_1} \\ U_\beta^{S_1} \\ U_\gamma^{S_1} \end{bmatrix} = & \begin{bmatrix} V_{g\alpha}^{S_1} & V_{g\beta}^{S_1} & 0 \\ -V_{g\beta}^{S_1} & V_{g\alpha}^{S_1} & 0 \\ 0 & 0 & V_{g\beta}^{S_1} - V_{g\alpha}^{S_1} \end{bmatrix} \begin{bmatrix} \bar{V}_\alpha^{S_1} \\ \bar{V}_\beta^{S_1} \\ \bar{V}_\gamma^{S_1} \end{bmatrix} \\ & - \begin{bmatrix} \left(V_{g\alpha}^{S_1}\right)^2 + \left(V_{g\beta}^{S_1}\right)^2 \\ 0 \\ 0 \end{bmatrix}. \end{aligned} \tag{10}$$

C. New Switching Times Calculation Method

The presented PDPC algorithms in [18]–[21] for three-leg converters use active and reactive powers' increments f_{p_i} and f_{q_i}. Then, the switching times are calculated based on the minimization of a cost function, which is defined as a sum of the square errors of the active and reactive powers. The resulting switching times' expressions depend on the active and reactive powers, their references, as well as the power increments f_{p_i} and f_{q_i}. The most drawback of this technique is that the calculated switching times can guarantee the convergence of the powers to their references only at the beginning and the end of each switching period. Therefore, within each switching period, the proposed PDPC in [18]–[21] cannot guarantee accurate power control, which can lead to a large ripple in the active and reactive powers.

In this section, the proposed switching time calculation method is explained; the proposed method can ensure accurate power control with reduced ripple during the entire switching period T_{sw}. Moreover, since the proposed predictive power model is defined in the first sector, the switching times are

calculated only for the SWVs located in the first sector, which leads to reduce the computational time of the proposed PDPC.

The main goal of the proposed PDPC is that the grid powers $p_g^{S_1}$, $q_g^{S_1}$, and $q_{g,\alpha\beta}^{S_1}$ will be forced to track their references, $p_g^{*S_1}$, $q_g^{*S_1}$, and $q_{g,\alpha\beta}^{*S_1}$. The grid powers can be calculated as in (4), just by using the components of the grid current $\vec{I}_g^{S_1}(I_{g\alpha}^{S_1},\ I_{g\beta}^{S_1},\ I_{g\gamma}^{S_1})$ instead of the components of the converter current $\vec{I}^{S_1}(I_\alpha^{S_1},\ I_\beta^{S_1},\ I_\gamma^{S_1})$ as follows:

$$\begin{bmatrix} p_g^{S_1} \\ q_g^{S_1} \\ q_{g,\alpha\beta}^{S_1} \end{bmatrix} = \begin{bmatrix} V_{g\alpha}^{S_1} & V_{g\beta}^{S_1} & 0 \\ -V_{g\beta}^{S_1} & V_{g\alpha}^{S_1} & 0 \\ 0 & 0 & V_{g\beta}^{S_1} - V_{g\alpha}^{S_1} \end{bmatrix} \begin{bmatrix} I_{g\alpha}^{S_1} \\ I_{g\beta}^{S_1} \\ I_{g\gamma}^{S_1} \end{bmatrix}. \tag{11}$$

In order to control the grid powers, the errors between the converter powers and their references in the new predictive power model of (9) can be replaced by the grid power errors as follows:

$$\begin{aligned} p_g^{*S_1}(k+1) - p_g^{S_1}(k) &= T_s\left(-R\,p_c^{S_1}(k) + U_\alpha^{S_1}(k)\right)/L \\ q_g^{*S_1}(k+1) - q_g^{S_1}(k) &= T_s\left(-R\,q_c^{S_1}(k) + U_\beta^{S_1}(k)\right)/L \\ q_{g,\alpha\beta}^{*S_1}(k+1) - q_{g,\alpha\beta}^{S_1}(k) &= T_s\left(-R\,q_{c,\alpha\beta}^{S_1}(k) + U_\gamma^{S_1}(k)\right)/L. \end{aligned} \tag{12}$$

The control input of the new predictive power model of (12) that can ensure the grid powers regulation is the reconstructed average output voltage vector $\vec{\bar{V}}^{S_1}(\bar{V}_\alpha^{S_1}\bar{V}_\beta^{S_1}\bar{V}_\gamma^{S_1})$, which is included in $\vec{U}^{S_1}(U_\alpha^{S_1}U_\beta^{S_1}U_\gamma^{S_1})$ as given in (10). With the aim of controlling the grid powers and to guarantee the operation with a CSF, the proposed PDPC applies, during each switching period, four appropriate SWVs only from the first sector S_1 and calculates their switching times to synthesize the vector $\vec{\bar{V}}^{S_1}$.

It is considered that $v_1^{S_1}, v_2^{S_1}, v_3^{S_1}$, and $v_4^{S_1}$ are the four appropriate SWVs from S_1 that should be applied during T_{sw}, and $t_1^{S_1}, t_2^{S_1}, t_3^{S_1},$ and $t_4^{S_1}$ are their corresponding switching times.

To get the accurate control of the active and reactive powers with reduced ripple during the entire switching period T_{sw}, the switching times are calculated based on the average value of the voltage vector during T_{sw} as follows:

$$\begin{aligned} v_1^{S_1}t_1^{S_1} + v_2^{S_1}t_2^{S_1} + v_3^{S_1}t_3^{S_1} + v_4^{S_1}t_4^{S_1} &= T_{sw}\vec{\bar{V}}^{S_1} \\ t_1^{S_1} + t_2^{S_1} + t_3^{S_1} + t_4^{S_1} &= T_{sw}. \end{aligned} \tag{13}$$

After decomposition in $\alpha\beta\gamma$ coordinates, (13) becomes as follows:

$$\begin{aligned} v_{1\alpha}^{S_1}t_1^{S_1} + v_{2\alpha}^{S_1}t_2^{S_1} + v_{3\alpha}^{S_1}t_3^{S_1} + v_{4\alpha}^{S_1}t_4^{S_1} &= T_{sw}\bar{V}_\alpha^{S_1} \\ v_{1\beta}^{S_1}t_1^{S_1} + v_{2\beta}^{S_1}t_2^{S_1} + v_{3\beta}^{S_1}t_3^{S_1} + v_{4\beta}^{S_1}t_4^{S_1} &= T_{sw}\bar{V}_\beta^{S_1} \\ v_{1\gamma}^{S_1}t_1^{S_1} + v_{2\gamma}^{S_1}t_2^{S_1} + v_{3\gamma}^{S_1}t_3^{S_1} + v_{4\gamma}^{S_1}t_4^{S_1} &= T_{sw}\bar{V}_\gamma^{S_1} \\ t_1^{S_1} + t_2^{S_1} + t_3^{S_1} + t_4^{S_1} &= T_{sw} \end{aligned} \tag{14}$$

where $v_{i\alpha}^{S_1}, v_{i\beta}^{S_1}$, and $v_{i\gamma}^{S_1}, (i = 1,\ 2,\ 3, \text{or } 4)$ are the components of the SWV $v_i^{S_1}$ in $\alpha\beta\gamma$ coordinates.

Using (14), the components of the reconstructed average output voltage vector $\vec{\bar{V}}^{S_1}(\bar{V}_\alpha^{S_1},\ \bar{V}_\beta^{S_1},\ \bar{V}_\gamma^{S_1})$ can be given as follows:

Using (15) and (10) in (12), the switching times can be calculated using the following expression:

$$\begin{aligned} &\begin{bmatrix} u_{1\alpha}^{S_1} - u_{4\alpha}^{S_1} & u_{2\alpha}^{S_1} - u_{4\alpha}^{S_1} & u_{3\alpha}^{S_1} - u_{4\alpha}^{S_1} \\ u_{1\beta}^{S_1} - u_{4\beta}^{S_1} & u_{2\beta}^{S_1} - u_{4\beta}^{S_1} & u_{3\beta}^{S_1} - u_{4\beta}^{S_1} \\ u_{1\gamma}^{S_1} - u_{4\gamma}^{S_1} & u_{2\gamma}^{S_1} - u_{4\gamma}^{S_1} & u_{3\gamma}^{S_1} - u_{4\gamma}^{S_1} \end{bmatrix} \begin{bmatrix} t_1^{S_1} \\ t_2^{S_1} \\ t_3^{S_1} \end{bmatrix} = \frac{T_{sw}L}{T_s} \begin{bmatrix} \Gamma_1 \\ \Gamma_2 \\ \Gamma_3 \end{bmatrix} \\ &t_4^{S_1} = T_{sw} - t_1^{S_1} - t_2^{S_1} - t_3^{S_1} \end{aligned} \tag{16}$$

with

$$\begin{bmatrix} \Gamma_1 \\ \Gamma_2 \\ \Gamma_3 \end{bmatrix} = \begin{bmatrix} p_g^{*S_1}(k+1) - p_g^{S_1}(k) + T_sR.p_c^{S_1}(k)/L - Lu_{4\alpha}^{S_1}/T_{sw} \\ q_g^{*S_1}(k+1) - q_g^{S_1}(k) + T_sR.q_c^{S_1}(k)/L - Lu_{4\beta}^{S_1}/T_{sw} \\ q_{g,\alpha\beta}^{*S_1}(k+1) - q_{g,\alpha\beta}^{S_1}(k) + T_sR.q_{c,\alpha\beta}^{S_1}(k)/L - Lu_{4\gamma}^{S_1}/T_{sw} \end{bmatrix} \tag{17}$$

where $u_{i\alpha}^{S_1},\ u_{i\beta}^{S_1},$ and $u_{i\gamma}^{S_1}(i = 1,\ 2,\ 3,\ or\ 4)$ are the intermediate SWVs components defined by

$$\begin{aligned} \begin{bmatrix} u_{i\alpha}^{S_1} \\ u_{i\beta}^{S_1} \\ u_{i\gamma}^{S_1} \end{bmatrix} &= \begin{bmatrix} V_{g\alpha}^{S_1} & V_{g\beta}^{S_1} & 0 \\ -V_{g\beta}^{S_1} & V_{g\alpha}^{S_1} & 0 \\ 0 & 0 & V_{g\beta}^{S_1} - V_{g\alpha}^{S_1} \end{bmatrix} \begin{bmatrix} \bar{V}_\alpha^{S_1} \\ \bar{V}_\beta^{S_1} \\ \bar{V}_\gamma^{S_1} \end{bmatrix} \\ &\quad - \begin{bmatrix} \left(V_{g\alpha}^{S_1}\right)^2 + \left(V_{g\beta}^{S_1}\right)^2 \\ 0 \\ 0 \end{bmatrix}. \end{aligned} \tag{18}$$

By calculating the switching times using (16) for the adjacent SWVs $v_1^{S_1}, v_2^{S_1}, v_3^{S_1}$, and $v_4^{S_1}$, the grid active and reactive powers

$$\begin{aligned} \bar{V}_\alpha^{S_1} &= v_{4\alpha}^{S_1} + \left[(v_{1\alpha}^{S_1} - v_{4\alpha}^{S_1})t_1^{S_1} + (v_{2\alpha}^{S_1} - v_{4\alpha}^{S_1})t_2^{S_1} + (v_{3\alpha}^{S_1} - v_{4\alpha}^{S_1})t_3^{S_1}\right]/T_{sw} \\ \bar{V}_\beta^{S_1} &= v_{4\beta}^{S_1} + \left[(v_{1\beta}^{S_1} - v_{4\beta}^{S_1})t_1^{S_1} + (v_{2\beta}^{S_1} - v_{4\beta}^{S_1})t_2^{S_1} + (v_{3\beta}^{S_1} - v_{4\beta}^{S_1})t_3^{S_1}\right]/T_{sw} \\ \bar{V}_\gamma^{S_1} &= v_{4\gamma}^{S_1} + \left[(v_{1\gamma}^{S_1} - v_{4\gamma}^{S_1})t_1^{S_1} + (v_{2\gamma}^{S_1} - v_{4\gamma}^{S_1})t_2^{S_1} + (v_{3\gamma}^{S_1} - v_{4\gamma}^{S_1})t_3^{S_1}\right]/T_{sw} \\ t_4^{S_1} &= T_{sw} - t_1^{S_1} - t_2^{S_1} - t_3^{S_1} \end{aligned} \tag{15}$$

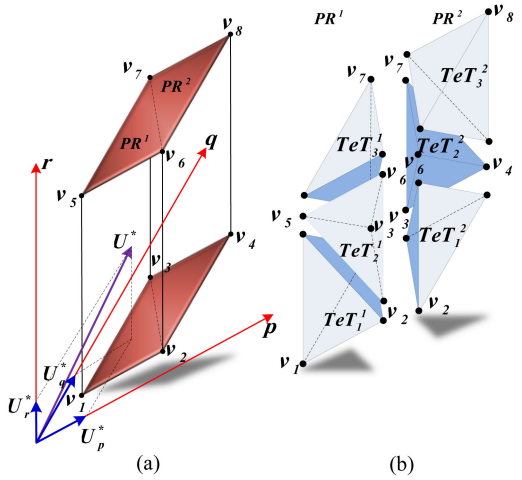

Fig. 4. (a) Three-dimensional parallelepiped. (b) Six types of tetrahedrons (TeT_i^j is the tetrahedron number i located in prism number j PR^j) [25].

will be forced to follow their references during each switching period T_{sw} with reduced ripple.

D. Generalized Approach for Appropriate SWVs Selection

As it is mentioned above, the reconstructed voltage vector $\vec{V}^{S_1}$ rotates only in the first sector S_1. Therefore, for any 4L-DCC level, the most appropriate SWVs that can be applied during each T_{sw} are those to be adjacent to the $\vec{V}^{S_1}$ when it rotates in S_1 of the SVD. The SVD of the m-level 4L-DCC is formed by tetrahedrons (TeTs) and each tetrahedron is composed of four SWVs. Therefore, in order to determine the four appropriate SWVs, it is necessary to identify the tetrahedron that contains $\vec{V}^{S_1}$. The method proposed in [25] is adopted in this article with some modifications to identify the tetrahedrons for any 4L-DCC level. In [25], new axes called ρ–σ–τ [see Fig. 4(a)] are used to identify the type of tetrahedron and to select the appropriate SWVs for m-level 4L-DCC. All tetrahedrons in S_1 of the SVD can be classified into six types [25], which can form two adjacent prisms (PR^1 and PR^2) (see Fig. 4). These adjacent prisms, in turn, constitute a 3-D parallelepiped having eight SWVs v_1, v_2, …, v_8 [25].

The normalized component of the $\vec{V}^{S_1}$ in $\rho\sigma\tau$ coordinates can be expressed as [25]

$$\begin{bmatrix} \bar{V}_\rho^{S_1} \\ \bar{V}_\sigma^{S_1} \\ \bar{V}_\tau^{S_1} \end{bmatrix} = \frac{m-1}{v_{\mathrm{dc}}} \begin{bmatrix} \sqrt{3/2} & -\sqrt{2}/2 & 0 \\ 0 & \sqrt{2} & 0 \\ -\sqrt{6}/6 & -\sqrt{2}/2 & \sqrt{3}/3 \end{bmatrix} \begin{bmatrix} \bar{V}_\alpha^{S_1} \\ \bar{V}_\beta^{S_1} \\ \bar{V}_\gamma^{S_1} \end{bmatrix}. \quad (19)$$

Based on the integer parts P, Q, and R of $\vec{V}^{S_1}$ components of (19), the coordinates of the SWVs of Fig. 4 can be deduced, as clarified in Table II.

Based on the fractional parts p, q, and r of $\vec{V}^{S_1}$ in (19), the tetrahedron type is easy to be identified for any 4L-DCC level [25].

Based on the tetrahedron type that contains $\vec{V}^{S_1}$ and the coordinates of the SWVs v_1, …, v_8, the appropriate SWVs for any 4L-DCC level can be generalized as given in Table III. The appropriate SWVs v_1^{S1}, v_2^{S1}, v_3^{S1}, and v_4^{S1} given in Table III are normalized in $\rho\sigma\tau$ coordinates. However, before using SWVs to calculate the switching times in (16) and (17), they should be denormalized and retransferred into $\alpha\beta\gamma$ using the reverse matrix transformation of (19).

Based on (19) and Table III, the appropriate SWVs are selected for any 4L-DCC level and they can be used to calculate the switching times as given in (16). After selecting the appropriate SWVs, the proposed method in [25] for generating and generalizing the switching sequence and balancing the dc capacitor voltages for m-level 4L-DCC is used in this article.

TABLE II
COORDINATES OF SWV IN $\rho\sigma\tau$ COORDINATES

SWV	Coordinates	SWV	Coordinates
$v_1(P_{v1},Q_{v1},R_{v1})$	(P, Q, R)	$v_5(P_{v5},Q_{v5},R_{v5})$	$(P, Q, R+1)$
$v_2(P_{v2},Q_{v2},R_{v2})$	$(P+1, Q, R)$	$v_6(P_{v6},Q_{v6},R_{v6})$	$(P+1, Q, R)$
$v_3(P_{v3},Q_{v3},R_{v3})$	$(P, Q+1, R)$	$v_7(P_{v7},Q_{v7},R_{v7})$	$(P, Q+1, R)$
$v_4(P_{v4},Q_{v4},R_{v4})$	$(P+1, Q+1, R)$	$v_8(P_{v8},Q_{v8},R_{v8})$	$(P+1, Q+1, R+1)$

TABLE III
GENERALIZED APPROACH FOR APPROPRIATE SWVS SELECTION FOR M-LEVEL 4L-DCC

PR^1	TeT_1^1	TeT_2^1	TeT_3^1
Appropriate SWVs $\left[v_1^{S1}\ v_2^{S1}\ v_3^{S1}\ v_4^{S1}\right]$	$[v_1\ v_2\ v_3\ v_5]$	$[v_6\ v_2\ v_3\ v_5]$	$[v_6\ v_7\ v_3\ v_5]$
PR^2	TeT_1^2	TeT_2^2	TeT_3^2
Appropriate SWVs $\left[v_1^{S1}\ v_2^{S1}\ v_3^{S1}\ v_4^{S1}\right]$	$[v_6\ v_2\ v_3\ v_4]$	$[v_6\ v_7\ v_3\ v_4]$	$[v_6\ v_7\ v_8\ v_4]$

TABLE IV
SYSTEM PARAMETERS

Parameter	Value
Grid RMS voltage and frequency	57 V, 50 Hz
Filtering impedance R and L	0.1 Ω, 3 mH
DC voltage v_{dc}	150 V
Sampling frequency f_s, switching frequency f_{sw}	100 kHz, 4 kHz

IV. RESULTS AND DISCUSSIONS

A. Simulation Results

In order to prove the effectiveness of the proposed generalized PDPC for m-level 4L-GCC, the simulation results under different 4L-DCC levels have been performed using the parameters, as listed in Table IV.

In order to validate the proposed generalized algorithm, the number of 4L-DCC level m is increased at each 50 ms. Fig. 5 shows the simulation results of the proposed generalized PDPC for different 4L-DCC levels (for $m = 2$, 3, 7, 11, and 15). From Fig. 5, it can be seen that the grid active/reactive power and line neutral current ripples are reduced by increasing the number of 4L-DCC level m. The quality of the line currents as well as the output voltage is improved, as demonstrated in Fig. 6, through the output voltage total harmonic distortion (THD) values.

Figs. 7 and 8 and Tables V and VI present a comprehensive comparative study between the proposed PDPC and the PDPC

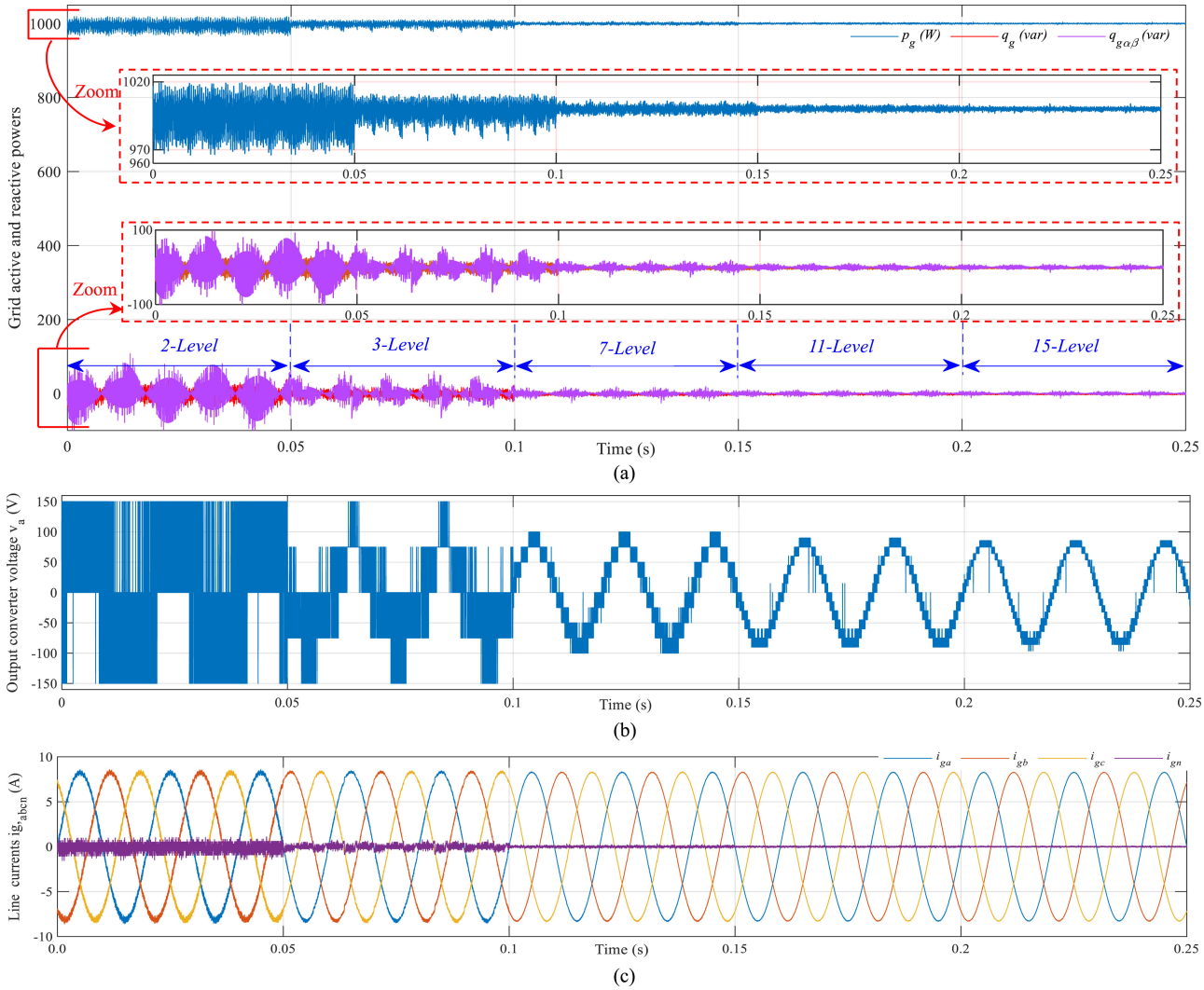

Fig. 5. Simulation results of the proposed generalized PDPC for different levels of the m-level 4L-DCC. (a) Grid active and reactive powers. (b) Output converter voltage v_a. (c) Line currents i_{ga}, i_{gb}, i_{gc}, and i_{gn}.

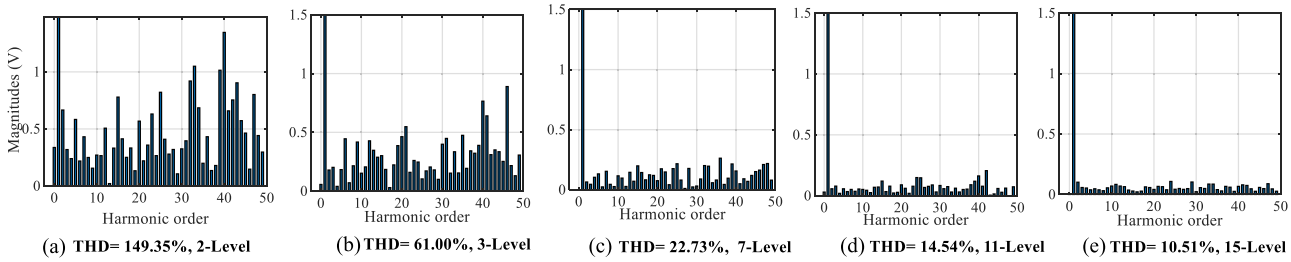

Fig. 6. Frequency spectrum of the output 4L-converter voltage. (a) 2-level. (b) 3-level. (c) 7-level 4L-DCC. (d) 11-level 4L-DCC. (e) 15-level 4L-DCC.

TABLE V
LINE CURRENT THD VERSUS COUPLING INDUCTANCE VALUE MISMATCH

		ΔL (%) = (L-L_c/L)×100										
		-100	-80	-60	-40	-20	0	20	40	60	80	100
THD (%)	Proposed PDPC	3	2.75	2.42	2.2	1.93	1.76	1.43	1.17	0.93	0.74	0.6
	PDPC in [18]–[21]	7.03	5.3	5.4	5.37	4.2	4.66	3.91	3.83	3.67	2.88	1.8

L_c is the inductance used in the control method, and L is the real value.

with CSF as per the articles presented in [18]–[21]. The comparison is performed based on the line current THD, active and reactive powers ripple, and line neutral current ripple.

In fact, the presented PDPCs in [18]–[21] were applied only for two- and three-level three-leg converters. Therefore, to perform a fair comparison with the proposed PDPC, the calculation time method that is used in [18]–[21] was applied to the proposed

TABLE VI
SIMULATION-BASED COMPARISON OF THE PROPOSED PDPC WITH THE EXISTING SCHEMES

		Proposed works				
		[26]	[27]	[28]	[29]	[30]
Converter level Control used		2-level 4-leg Model Predictive Current Control	3-level 3-leg Model Predictive Current Control	2-level 3-leg DPC-PWM	3-level 4-leg Hybrid DPC/current with PI controller	2-level 4-leg Hysteresis Current Controller
Application		GCC	GCC	GCC	SAPF	SAPF
Switching frequency		Variable --	Variable Average of 5 kHz	Constant 10 kHz	Constant 5 kHz	Variable Average of 10 kHz
THD (%)	Previous works	0.39	13.53	1.2	2.77	3.02
	Proposed PDPC	0.23	10.26	0.52	0.43	2.30

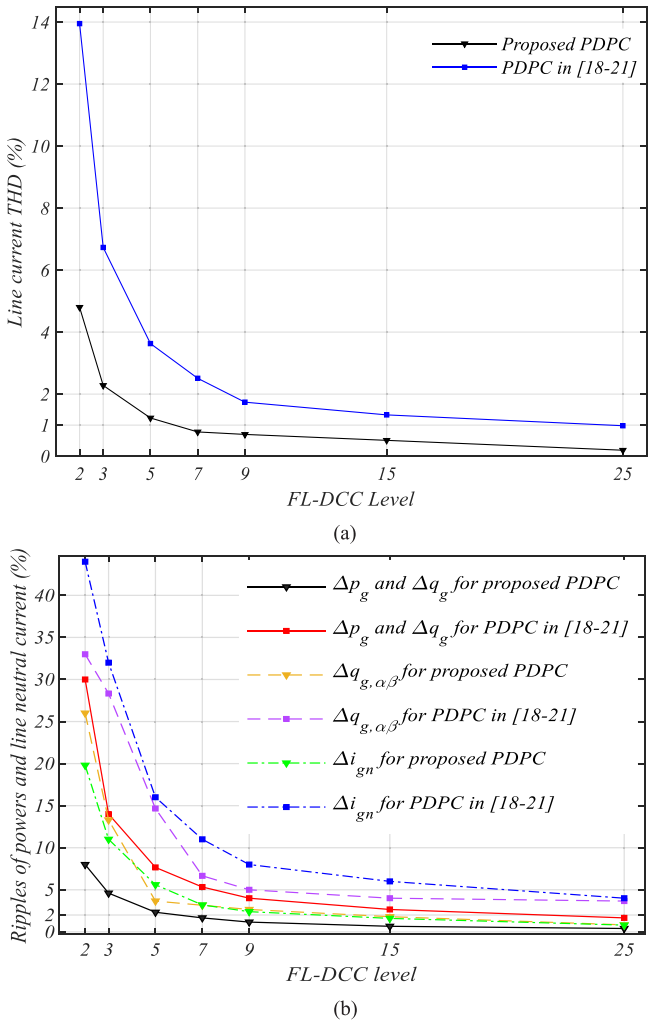

Fig. 7. Comparative investigation between the proposed PDPC and the presented PDPC in [18]–[21] for different 4L-DCC levels. (a) Line current THD. (b) Ripple of grid powers and line neutral current.

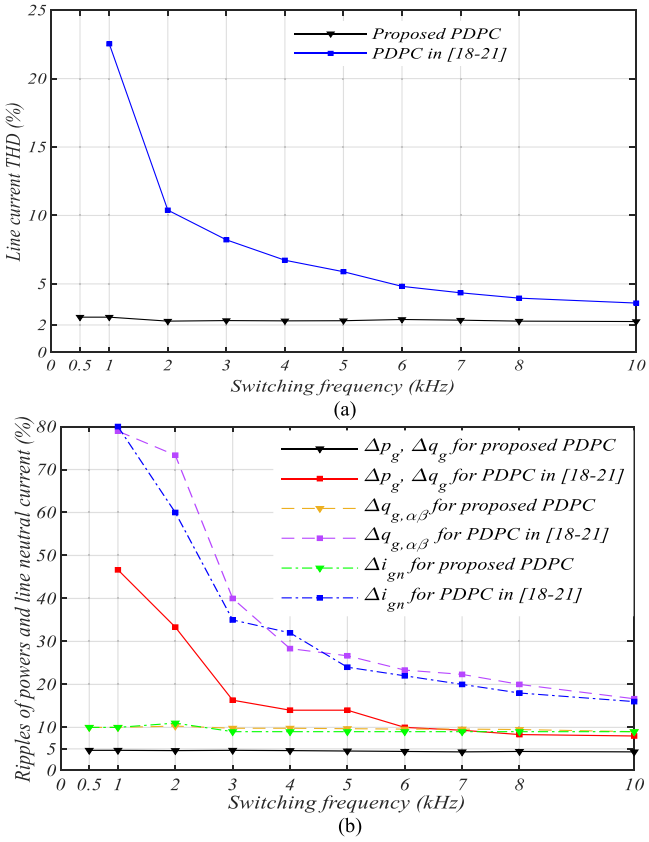

Fig. 8. Comparative investigation between the proposed PDPC and the presented PDPC in [18]–[21] for three-level 4L-DCC under different switching frequency values. (a) Line current THD. (b) Ripple of grid powers/line neutral current.

PDPC algorithm and was generalized for m-level 4L-GCC using the proposed generalized approach.

Fig. 7 shows the simulation values of the line current THD, grid active and reactive powers ripple (%) Δp_g, Δq_g, $\Delta p_{g,\alpha\beta}$, and line neutral current ripple Δi_{gn} (%) versus different 4L-DCC levels with $p_g = 1$ kW and $f_s = 4$ kHz. It is clear that the line current THD and the grid power/line neutral current ripple are decreased with increasing the number of 4L-DCC levels. However, the proposed PDPC shows the reduced values of power ripples and current THD compared with the PDPC proposed in [18]–[21], especially for lower levels of the 4L-DCC.

Fig. 8 shows the line current THD and the ripple of the grid power/line neutral current versus the switching frequency for three-level 4L-DCC. Obviously, the THD and ripple values are almost independent of the switching frequency of the proposed PDPC. The proposed PDPC can operate with low switching frequency values (0.5 and 1 kHz), which proves its effectiveness compared with the PDPC proposed in [18]–[21].

Table V lists the line current THD variation under coupling inductance value mismatch for the proposed PDPC and the PDPC algorithms presented in [18]–[21]. It can be noticed that the proposed PDPC algorithm has a small sensitivity to mismatch in the inductance L. The THD can be kept at reduced

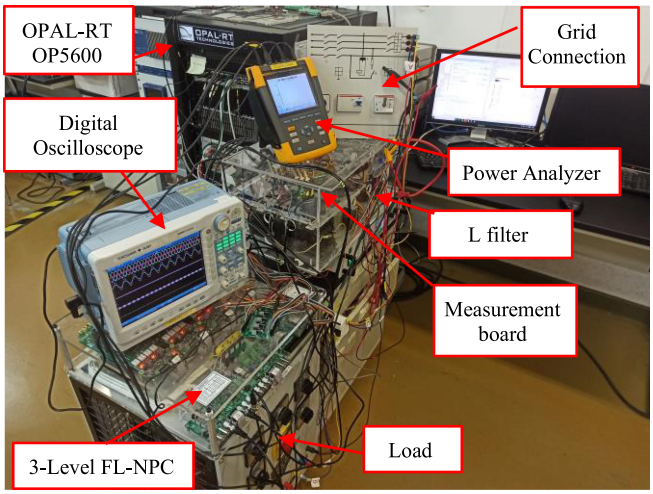

Fig. 9. Experimental setup of the three-level 4L-DCC.

value (less than 3%) when an extreme mismatch is applied $|\Delta L|$ ($\pm 100\%$).

Table VI lists a comparative investigation based on the line current THD of the proposed PDPC and recently proposed control schemes [26]–[30]. The comparison was made in the same application [GCC or shunt active power filter (SAPF)] and the same parameters between the proposed PDPC and each previous work from the articles presented in [26]–[30] (the same supply system, load, filtering impedance, converter level, switching frequency, operating condition, etc.). This comparison proves the effectiveness of the proposed control method in terms of the line current quality improvement.

B. Experimental Results

In this section, the experimental results of the proposed PDPC for the three-level 4L-DCC are presented. The OPAL-RT OP5600 real-time controller is used to implement the proposed control strategy for the hardware prototype, as shown in Fig. 9. The parameters used in the experimental setup are similar to those used in the simulation section. Moreover, the dc voltage in this case is $v_{\rm dc} = 200$ V, the dc-link capacitances are $C_1 = C_2 = 340$ μF, and an additional three-phase inductive load is connected at the point of common coupling (PCC) side with $(R_L, L_L) = (45\ \Omega, 20$ mH).

The proposed PDPC was investigated experimentally for the three-level 4L-DCC under the following testing scenarios:

1) step change of grid powers (see Fig. 10);
2) unbalanced grid voltage condition [see Fig. 11(a)];
3) distorted grid voltage condition [see Fig. 11(b)];
4) unbalanced current condition (see Fig. 12).

1) Reference Active and Reactive Powers Variation: In Fig. 10, the behavior of the system is illustrated when a step change of the grid powers p_g and q_g is applied. As can be seen, the proposed PDPC can smoothly follow the step changes in the power references, the grid active power p_g varies from 500 to 1000 W, the reactive power q_g is increased from 0 to 400 var, while the reactive power $q_{g,\alpha\beta}$ is kept at zero level to maintain the line currents balanced. At the instant of increasing p_g from

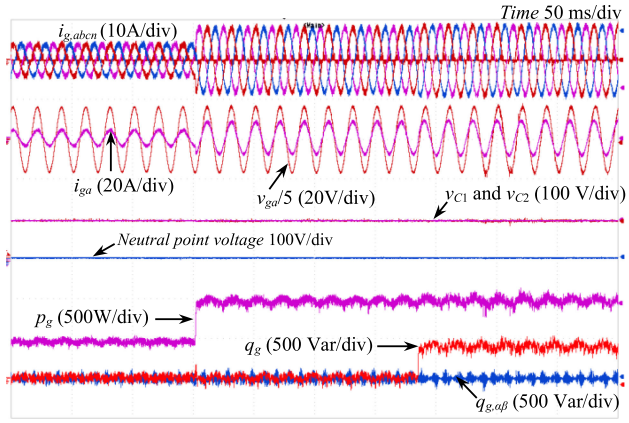

Fig. 10. Experimental results under step change of the grid active and reactive powers using the proposed PDPC for three-level 4L-DCC (p_g is changed from 500 to 1000 W, and q_g from 0 to 400 var).

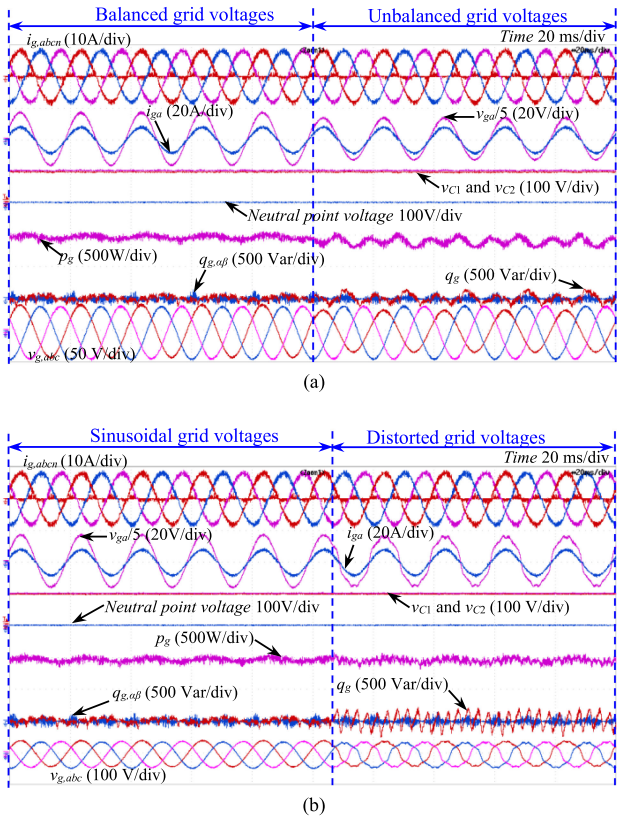

Fig. 11. Experimental results of the proposed PDPC for three-level 4L-GCC with $p_g = 1000$ W, $q_g = 0$ var under (a) unbalanced grid voltages and (b) distorted grid voltages.

500 to 1000 W, the system reacts by doubling the amplitude of the line currents to 8 A. On the other hand, the step change of q_g from 0 to 400 var forces the line current i_{ga} to be ahead with respect to the corresponding grid voltage v_{ga}. The dc capacitor voltages are kept balanced even during the power changes.

2) Unbalanced/Distorted Grid Voltage Condition: With the aim to test the proposed PDPC performance under abnormal conditions, a grid emulator is used to generate unbalanced voltages (20% sag in phase a [see Fig. 11(a)]) as well as to

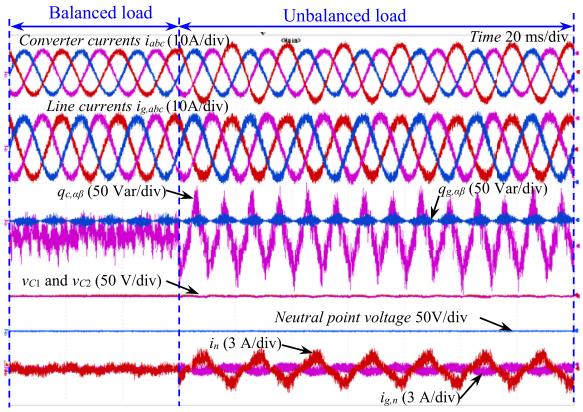

Fig. 12. Experimental results under unbalanced load condition of the proposed PDPC for three-level 4L-DCC with $p_g = 1000$ W and $q_g = 0$.

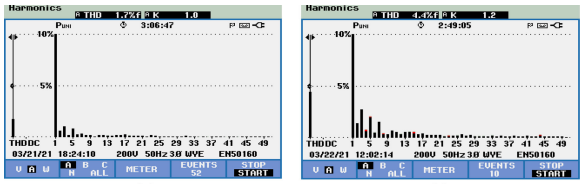

(a) (b)

Fig. 13. Frequency spectrum of the line current under steady-state operation with $p_g = 1000$ W. (a) Using proposed PDPC. (b) Using PDPC proposed in [18]–[21].

TABLE VII
EXPERIMENTAL LINE CURRENT THD UNDER DIFFERENT OPERATING CONDITIONS FOR THE PROPOSED PDPC

Operating condition	Steady-state		Distorted grid voltages	Unbalanced grid voltages
p_g(W)	500	1000	1000	1000
THD (%)	2.2	1.7	1.9	2.1

deliver distorted voltages [see Fig. 11(b)]. The fundamental voltage components are superimposed with 8.5% of the 3rd harmonic, 7% of 5th harmonic, 5% of 7th harmonic, and 2.5% of 11th harmonic. Fig. 11 shows the results under unbalanced and distorted voltages. It can be observed that the active and reactive powers have a small ripple due to the distorted and unbalanced grid voltages; meanwhile, the proposed PDPC can deal with any disturbances effectively and ensure balanced and sinusoidal line currents. The line current THD is 1.9% and 2.1% in the case of distorted and unbalanced grid voltage conditions, respectively (see Table VII). Moreover, the neutral point voltage at the dc side is almost zero and the dc capacitor voltages are maintained balanced even during the grid voltage disturbances.

3) Unbalanced Current Condition: As shown in Fig. 12, the dynamic response of the PDPC strategy is studied under unbalanced currents. In this case, a three-phase inductive load of (45 Ω, 20 mH) is connected at the PCC side. In order to create an unbalanced load, an additional inductive load of (45 Ω, 20 mH) is connected in parallel with phase *a*. The active power reference is set to 1000 W. At the moment of connecting the unbalanced load, the 4L-DCC reacts by injecting the required reactive power $q_{c,\alpha\beta}$ with an oscillating component to keep the grid reactive power $q_{g,\alpha\beta}$ around zero. Thus, the line currents are maintained balanced and the line neutral current i_{gn} is compensated. The dc capacitor voltages are preserved at the desired level of $v_{\rm dc}/2$ even with the unbalanced converter currents.

Table VII lists the experimental values of the line current THD obtained with the proposed PDPC under different operating conditions, where the quality of the line current THD is kept within the international standards intervals (THD less than 2.2%).

Fig. 13 shows the experimental frequency spectra of the line current obtained under steady-state operation with $p_g = 1$ kW for the proposed PDPC and the PDPC proposed in [18]–[21]. It can be observed that the proposed PDPC improves the line current quality with a THD of 1.7% compared with the PDPC proposed in [18]–[21], which provides a THD of 4.4%.

The computational time for both proposed PDPC and the other algorithms proposed in [18]–[21] has been measured in real time using the real-time controller OP5600. The PDPC presented in [18]–[21] requires 1.7 μs, while the proposed in this article PDPC needs 1.5 μs, which demonstrates the effectiveness of the proposed solution in terms of reducing the computational burden.

V. CONCLUSION

This article proposed a novel generalized PDPC operated with a CSF for multilevel 4L-DCC connected to the grid without using any modulation stage. In this article, a new predictive power model for 4L-GCC was developed. The proposed algorithm selects four SWVs from the first sector of the SVD only to be applied to switching times calculation for each switching period. Moreover, it offers a new and generalized method to calculate the switching times of the corresponding SWVs. All stages of the proposed PDPC algorithm were generalized to be applied for any level of the 4L-DCC. The conducted simulation and experimental results prove the effectiveness and the superiority of the proposed PDPC algorithm in terms of the active/reactive power control, current quality improvement, and neutral current compensation.

ACKNOWLEDGMENT

The statements made herein are solely the responsibility of the authors.

REFERENCES

[1] H. Abu-Rub, J. Holtz, J. Rodriguez, and G. Baoming, "Medium-voltage multilevel converters—State of the art, challenges, and requirements in industrial applications," *IEEE Trans. Ind. Electron.*, vol. 57, no. 8, pp. 2581–2596, Aug. 2010, doi: 10.1109/TIE.2010.2043039.

[2] M. Malinowski, K. Gopakumar, J. Rodriguez, and M. A. Perez, "A survey on cascaded multilevel inverters," *IEEE Trans. Ind. Electron.*, vol. 57, no. 7, pp. 2197–2206, Jul. 2010, doi: 10.1109/TIE.2009.2030767.

[3] M.-J. Tsai, H.-C. Chen, and P.-T. Cheng, "Eliminating the neutral-point oscillation of the four-wire NPC active power filter," *IEEE Trans. Power Electron.*, vol. 34, no. 7, pp. 6233–6240, Jul. 2019, doi: 10.1109/TPEL.2018.2873258.

[4] E. Espina, R. Cárdenas-Dobson, M. B. Espinoza, C. Burgos-Mellado, and D. Saez, "Cooperative regulation of imbalances in three-phase four-wire microgrids using single-phase droop control and secondary control algorithms," *IEEE Trans. Power Electron.*, vol. 35, no. 2, pp. 1978–1992, Feb. 2020, doi: 10.1109/TPEL.2019.2917653.

[5] C. Burgos-Mellado, R. Cardenas, D. Saez, A. Costabeber, and M. Sumner, "A control algorithm based on the conservative power theory for cooperative sharing of imbalances in four-wire systems," *IEEE Trans. Power Electron.*, vol. 34, no. 6, pp. 5325–5339, Jun. 2019, doi: 10.1109/TPEL.2018.2869866.

[6] X. Guo, Y. Yang, B. Wang, and F. Blaabjerg, "Leakage current reduction of three-phase Z-source three-level four-leg inverter for transformerless PV system," *IEEE Trans. Power Electron.*, vol. 34, no. 7, pp. 6299–6308, Jul. 2019, doi: 10.1109/TPEL.2018.2873223.

[7] H. Komurcugil, S. Bayhan, and H. Abu-Rub, "Variable- and fixed-switching-frequency-based HCC methods for grid-connected VSI with active damping and zero steady-state error," *IEEE Trans. Ind. Electron.*, vol. 64, no. 9, pp. 7009–7018, Sep. 2017, doi: 10.1109/TIE.2017.2686331.

[8] H. Abu-Rub, J. Guziński, Z. Krzeminski, and H. A. Toliyat, "Predictive current control of voltage-source inverters," *IEEE Trans. Ind. Electron.*, vol. 51, no. 3, pp. 585–593, Jun. 2004, doi: 10.1109/TIE.2004.825364.

[9] M. Malinowski, M. P. Kazmierkowski, S. Hansen, F. Blaabjerg, and G. D. Marques, "Virtual-flux-based direct power control of three-phase PWM rectifiers," *IEEE Trans. Ind. Appl.*, vol. 37, no. 4, pp. 1019–1027, Jul./Aug. 2001, doi: 10.1109/28.936392.

[10] M. Malinowski, M. Jasiński, and M. P. Kazmierkowski, "Simple direct power control of three-phase PWM rectifier using space-vector modulation (DPC-SVM)," *IEEE Trans. Ind. Electron.*, vol. 51, no. 2, pp. 447–454, Apr. 2004, doi: 10.1109/TIE.2004.825278.

[11] S. Yan, J. Chen, T. Yang, and S. Y. Hui, "Improving the performance of direct power control using duty cycle optimization," *IEEE Trans. Power Electron.*, vol. 34, no. 9, pp. 9213–9223, Sep. 2019, doi: 10.1109/TPEL.2018.2883425.

[12] Y. Zhang, J. Jiao, and D. Xu, "Direct power control of doubly fed induction generator using extended power theory under unbalanced network," *IEEE Trans. Power Electron.*, vol. 34, no. 12, pp. 12024–12037, Dec. 2019, doi: 10.1109/TPEL.2019.2906013.

[13] R. Sadeghi, S. M. Madani, M. Ataei, M. R. Agha Kashkooli, and S. Ademi, "Super-twisting sliding mode direct power control of a brushless doubly fed induction generator," *IEEE Trans. Ind. Electron.*, vol. 65, no. 11, pp. 9147–9156, Nov. 2018, doi: 10.1109/TIE.2018.2818672.

[14] Y. Gui, G. H. Lee, C. Kim, and C. C. Chung, "Direct power control of grid connected voltage source inverters using port-controlled Hamiltonian system," *Int. J. Control, Autom. Syst.*, vol. 15, no. 5, pp. 2053–2062, Oct. 2017, doi: 10.1007/s12555-016-0521-9.

[15] J. Rodriguez *et al.*, "State of the art of finite control set model predictive control in power electronics," *IEEE Trans. Ind. Informat.*, vol. 9, no. 2, pp. 1003–1016, May 2013, doi: 10.1109/TII.2012.2221469.

[16] X. Wang *et al.*, "Novel model predictive direct power control strategy for grid-connected three-level inverters," *IET Power Electron.*, vol. 13, no. 16, pp. 3727–3733, Dec. 2020, doi: 10.1049/iet-pel.2020.0038.

[17] A. Benzouaoui, H. Khouidmi, and B. Bessedik, "Parallel model predictive direct power control of DFIG for wind energy conversion," *Int. J. Elect. Power Energy Syst.*, vol. 125, Feb. 2021, Art. no. 106453, doi: 10.1016/j.ijepes.2020.106453.

[18] S. Aurtenechea Larrinaga, M. A. Rodríguez Vidal, E. Oyarbide, and J. R. Torrealday Apraiz, "Predictive control strategy for dc/ac converters based on direct power control," *IEEE Trans. Ind. Electron.*, vol. 54, no. 3, pp. 1261–1271, Jun. 2007, doi: 10.1109/TIE.2007.893162.

[19] G. Abad, M. Á. Rodríguez, and J. Poza, "Two-level VSC-based predictive direct power control of the doubly fed induction machine with reduced power ripple at low constant switching frequency," *IEEE Trans. Energy Convers.*, vol. 23, no. 2, pp. 570–580, Jun. 2008, doi: 10.1109/TEC.2007.914167.

[20] P. Antoniewicz and M. P. Kazmierkowski, "Virtual-flux-based predictive direct power control of ac/dc converters with online inductance estimation," *IEEE Trans. Ind. Electron.*, vol. 55, no. 12, pp. 4381–4390, Dec. 2008, doi: 10.1109/TIE.2008.2007519.

[21] M. E. Zarei, C. V. Nicolas, J. R. Arribas, and D. Ramirez, "Four-switch three-phase operation of grid-side converter of doubly fed induction generator with three vectors predictive direct power control strategy," *IEEE Trans. Ind. Electron.*, vol. 66, no. 10, pp. 7741–7752, Oct. 2019, doi: 10.1109/TIE.2018.2880672.

[22] A. Krama, L. Zellouma, B. Rabhi, S. S. Refaat, and M. Bouzidi, "Real-time implementation of high performance control scheme for grid-tied PV system for power quality enhancement based on MPPC-SVM optimized by PSO algorithm," *Energies*, vol. 11, no. 12, 2018, Art. no. 3516, doi: 10.3390/en11123516.

[23] A. Krama, L. Zellouma, A. Benaissa, B. Rabhi, M. Bouzidi, and M. F. Benkhoris, "Design and experimental investigation of predictive direct power control of three-phase shunt active filter with space vector modulation using anti-windup proportional integral (PI) controller optimized by PSO," *Arab. J. Sci. Eng.*, vol. 44, no. 8, pp. 6741–6755, 2019, doi: 10.1007/s13369-018-3611-6.

[24] J. R. Fischer, S. A. Gonzalez, I. Carugati, M. A. Herran, M. G. Judewicz, and D. O. Carrica, "Robust predictive control of grid-tied converters based on direct power control," *IEEE Trans. Power Electron.*, vol. 29, no. 10, pp. 5634–5643, Oct. 2014, doi: 10.1109/TPEL.2013.2294919.

[25] M. Bouzidi, S. Barkat, and A. Krama, "New simplified and generalized three-dimensional space vector modulation algorithm for multilevel four-leg diode clamped converter," *IEEE Trans. Ind. Electron.*, vol. 68, no. 10, pp. 9908–9918, Oct. 2021, doi: 10.1109/TIE.2020.3026298.

[26] B. Long, T. Cao, W. Fang, K. T. Chong, and J. M. Guerrero, "Model predictive control of a three-phase two-level four-leg grid-connected converter based on sphere decoding method," *IEEE Trans. Power Electron.*, vol. 36, no. 2, pp. 2283–2297, Feb. 2021, doi: 10.1109/TPEL.2020.3006432.

[27] A. Calle-Prado, S. Alepuz, J. Bordonau, J. Nicolas-Apruzzese, P. Cortés, and J. Rodriguez, "Model predictive current control of grid-connected neutral-point-clamped converters to meet low-voltage ride-through requirements," *IEEE Trans. Ind. Electron.*, vol. 62, no. 3, pp. 1503–1514, Mar. 2015, doi: 10.1109/TIE.2014.2364459.

[28] Y. Gui, X. Wang, H. Wu, and F. Blaabjerg, "Voltage-modulated direct power control for a weak grid-connected voltage source inverters," *IEEE Trans. Power Electron.*, vol. 34, no. 11, pp. 11383–11395, Nov. 2019, doi: 10.1109/TPEL.2019.2898268.

[29] M. Bouzidi, A. Benaissa, and S. Barkat, "Hybrid direct power/current control using feedback linearization of three-level four-leg voltage source shunt active power filter," *Int. J. Electr. Power Energy Syst.*, vol. 61, pp. 629–646, 2014, doi: 10.1016/j.ijepes.2014.03.071.

[30] N. M. Ismail and M. K. Mishra, "Study on the design and switching dynamics of hysteresis current controlled four-leg voltage source inverter for load compensation," *IET Power Electron.*, vol. 11, no. 2, pp. 310–319, Feb. 2018, doi: 10.1049/iet-pel.2017.0118.

Mansour Bouzidi (Member, IEEE) was born in M'sila, Algeria, in 1985. He received the B.Eng. degree in electrical engineering from M'sila University, M'Sila, Algeria, in 2009, and the M.S. and Ph.D. degrees in power electronics from the Djillali Liabes University of Sidi-Bel-Abbes, Sidi Bel Abbès, Algeria, in 2011 and 2017, respectively.

Since 2012, he has been an Associate Professor with the Kasdi Merbah University of Ouargla, Ouargla, Algeria. His current research interests include power electronics, renewable energy conversion, and electrical drives.

Said Barkat received the Ph.D. degree in electrical engineering from the National Polytechnic School of Algiers, El Harrach, Algeria, in 2008.

In 2000, he joined the Faculty of Technology with M'sila University, M'Sila, Algeria, where he is currently a Full Professor with Electrical Engineering Department. His research interests include renewable energy conversion, power electronics, and advanced control theory and applications.

Abdelbasset Krama (Member, IEEE) received the bachelor's and master's (Hons.) degrees from the Kasdi Merbah University of Ouargla, Ouargla, Algeria, in 2013 and 2015, respectively, and the Ph.D. degree from El-Oued University, El-Oued, Algeria, in 2019, all in electrical engineering.

From 2017 to 2018, he was an Assistant Lecturer with the University of Ouargla. In October 2018, he joined as a Research Assistant with the Department of Electrical and Computer Engineering, Texas A&M University at Qatar, Doha, Qatar, where he was promoted to a Research Associate in June 2019. Since April 2020, he has been a Postdoctoral Research Associate with the Department of Electrical and Computer Engineering, Texas A&M University at Qatar. His current research interests include power quality, power electronics converters, and renewable energy conversion.

Dr. Krama is a Professional Active Member of the IEEE Industrial Electronics Society. He is currently the Secretary of the IEEE Qatar Chapter. He is also a reviewer for a number of IEEE journals and conferences.

Haitham Abu-Rub (Fellow, IEEE) received the M.Sc. degree in electrical engineering from Gdynia Maritime University, Gdynia, Poland, in 1990, the Ph.D. degree in electrical engineering from the Gdansk University of Technology, Gdansk, Poland, in 1995, and the second Ph.D. degree in humanities from Gdansk University, Gdansk, Poland, in 2004.

He is a Professor with Texas A&M University at Qatar (TAMUQ). He has research and teaching experiences at many universities in many countries, including Qatar, Poland, Palestine, USA, and Germany. He has served for five years as the Chair of Electrical and Computer Engineering Program with TAMUQ, where he is serving as the Managing Director of the Smart Grid Center. His main research interests include power electronic converters, renewable energy systems, electric drives, and smart grid. He has authored or coauthored more than 500 journal and conference papers, six books, and six book chapters.

Dr. Abu-Rub is the recipient of many national and international awards and recognitions. He is the Co-Editor in Chief for the IEEE TRANSACTIONS ON INDUSTRIAL ELECTRONICS.